ARTICLE

Shedding light on ultrafast ring-twisting pathways of halogenated GFP chromophores from the excited to ground state

Sean A. Boulanger,[a] Cheng Chen,[a] Longteng Tang,[a] Liangdong Zhu,[a] Nadezhda S. Baleeva,[b,c] Ivan N. Myasnyanko,[b,c] Mikhail S. Baranov,[b,c] and Chong Fang*[a]

Since green fluorescent protein (GFP) has revolutionized molecular and cellular biology for about three decades, there has been a keen interest in understanding, designing, and controlling the fluorescence properties of GFP chromophore (i.e., HBDI) derivatives from the protein matrix to solution. Amongst these cross-disciplinary efforts, the elucidation of excited-state dynamics of HBDI derivatives holds the key to correlating the light-induced processes and fluorescence quantum yield (FQY). Herein, we implement steady-state electronic spectroscopy, femtosecond transient absorption (fs-TA), femtosecond stimulated Raman spectroscopy (FSRS), and quantum calculations to study a series of mono- and dihalogenated HBDI derivatives (X=F, Cl, Br, 2F, 2Cl, and 2Br) in basic aqueous solution, gaining new insights into the photophysical reaction coordinates. In the excited state, the halogenated "floppy" chromophores exhibit an anti-heavy atom effect, reflected by strong correlations between FQY vs. Franck-Condon energy (E_{FC}) or Stokes shift, and k_{nr} vs. E_{FC}, as well as swift bifurcation into the I-ring (major) and P-ring (minor) twisting motions. In the ground state, both ring-twisting motions become more susceptible to sterics and exhibit spectral signatures from the halogen-dependent hot ground-state absorption band decay in TA data. We envision this type of systematic analysis of the halogenated HBDI derivatives to provide guiding principles for the site-specific modification of GFP chromophores, and expand design space for brighter and potentially photoswitchable organic chemical probes in aqueous solution with discernible spectral signatures throughout the photocycle.

Received 00th January 20xx,
Accepted 00th January 20xx

DOI: 10.1039/x0xx00000x

Introduction

The Pacific Northwest native jellyfish *Aequorea victoria* has possessed an intrinsic bioluminescent protein for over 160 million years. However, the discovery of this bright green fluorescent protein (GFP) did not occur until 1962 when Shimomura et al. extracted, purified, and characterized GFP that crowned the 2008 Nobel Prize in Chemistry.[1-4] Inspired and motivated by pioneering work of Chalfie and Tsien, the other two Nobel Laureates for GFP,[2,4,5] numerous FPs have since been engineered with fluorescence color ranging from blue to far-red, and the site-specific mutation properties have been characterized.[6-14] Inspired by GFP, the ability for fluorescent labeling of proteins has been greatly expanded from genetically encodable tags, organic fluorophores, to quantum dots. Each of these labels have advantages and disadvantages and must be strategically chosen on the basis of the scientific problem under investigation. In essence, the emission brightness, wavelength and lifetime, Stokes shift, size, and photostability are the dominant intrinsic traits for ideal fluorescent probes.[13,15-18]

Organic fluorophores can be tactically engineered to have certain advantages over FPs, such as a wider spectral range, higher brightness, and greater robustness. Size also plays a pivotal role in their functions. The relatively large FPs (~30 kDa) may be bulkier than a targeted protein and tend to oligomerize into dimers or tetramers, whereas small fluorophores are less likely to perturb biological activity, as long as electrostatic properties of the labeled analyte are not altered too much.[16] However, the compact molecular size of an organic fluorophore may pose some issues for tuning its electronic properties to obtain a redder emission, because the most common approach is extension of the π-conjugation.[19,20] One biomimetic strategy is thus to understand and then generate GFP chromophore derivatives that work well in solution, so we could efficiently expand the functional space of organic fluorophores with desirable properties from size, brightness, to emission color.

Notably, the three-residue-chromophore (Ser65-Tyr66-Gly67) responsible for strong green-light-emitting properties of wild-type (wt)GFP is formed by an autocatalytic cyclization and oxidation reaction in the protein matrix.[21,22] The resultant

[a] *Department of Chemistry, Oregon State University, 153 Gilbert Hall, Corvallis, Oregon 97331-4003, USA. E-mail: Chong.Fang@oregonstate.edu; Web: https://fanglab.oregonstate.edu/; Fax: +1 541 737 2062; Tel: +1 541 737 6704*
[b] *Institute of Bioorganic Chemistry, Russian Academy of Sciences, Miklukho-Maklaya 16/10, Moscow 117997, Russia*
[c] *Pirogov Russian National Research Medical University, Ostrovitianov 1, Moscow 117997, Russia*

† Electronic Supplementary Information (ESI) available: Synthesis methods of new mono- and dihalogenated HBDI derivatives, ESI Fig. S1–S8, Tables S1–S6, and Appendix S1–S2 with additional discussions on the steady-state and time-resolved spectroscopic (both fs-TA and FSRS) data, pK_a titration curves, computational results and vibrational mode assignments in both S_0 and S_1 states, Strickler-Berg equation data, natural bond orbital charges, and references. See DOI: 10.1039/x0xx00000x

fluorescence quantum yield (FQY) of $\Phi \approx 0.8$ arises from the anionic chromophore through ultrafast excited-state proton transfer (ESPT), which originates from a photoexcited neutral chromophore to its surroundings.[7,21-24] Outside of the protein pocket, model GFP chromophore 4-hydroxybenzylidene-1,2-dimethylimidazolinone (*p*-HBDI) becomes essentially non-fluorescent ($\Phi \approx 1 \times 10^{-4}$) in both anionic (see Table 1 below) and neutral forms, which has prompted many steady-state and time-resolved spectroscopic investigations.[25-29]

The short-lived excited state of *p*-HBDI is governed by ultrafast nonradiative *cis-trans* isomerization to reach the electronic hot ground state (hot-GS) through a nonadiabatic conical intersection (CI) deactivation and/or internal conversion (IC) pathway, which could outcompete ESPT reaction.[26,27,30,31] The photophysical properties of the unlocked *p*-HBDI and its derivatives mainly involve isomerization around the methine bridge C=C or C–C bond, whereas the volume-conserving hula-twist motion was deemed unlikely by high-level quantum calculations.[28,32,33] Attempts to increase the ESPT efficiency and FQY amongst HBDI derivatives, without drastically increasing its size, have been explored.[34,35] We have recently implemented a "double-donor-one-acceptor" strategy to effectively red-shift the emission of GFP chromophore derivatives,[18] wherein a coordination-assisted borylation reaction locks the phenolic (P, donor) and imidazolinone (I, acceptor) rings to increase the FQY in solution, while electron-donating groups (EDGs) on the donor and electron-withdrawing groups (EWGs) on the acceptor moieties can synergistically tune the emission wavelength.[36]

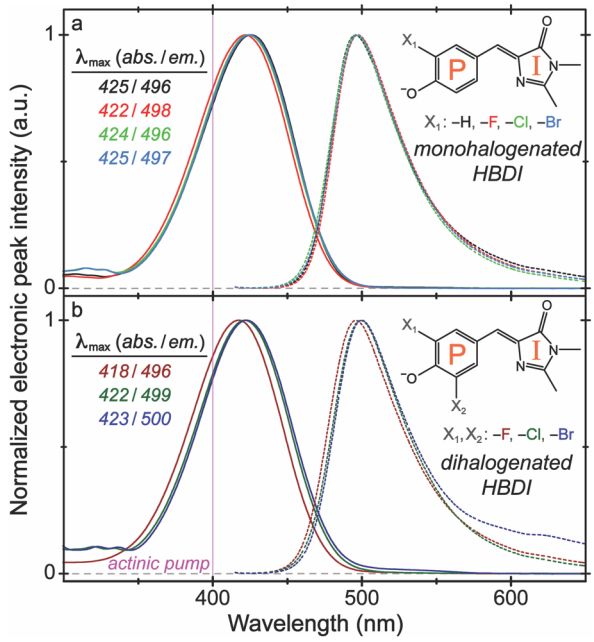

Fig. 1 Chemical structures and steady-state electronic spectroscopy of the anionic (a) *p*-HBDI, monohalogenated and (b) dihalogenated HBDI derivatives in aqueous solution. The absorption/emission peak maxima values are color-coded according to the substituents (hydrogen, H, black; fluorine, F, red; chlorine, Cl, green; bromine, Br, blue; 2F, dark red; 2Cl, dark green; and 2Br, dark blue). The P- and I-rings are labeled in orange. The magenta vertical line represents the 400 nm actinic pump for fs-TA and excited-state FSRS experiments.

Moreover, a more photoacidic fluorophore could increase the ESPT rate, Stokes shift, and intramolecular charge transfer (ICT) upon electronic excitation of the chromophore in solution.[37-40]

Halogenation is not typically integrated into the design of fluorescent chromophores due to their small size and high electronegativity. Fluorescence quenching upon halogenation due to heavy atom effect (HAE) was reported, which enhances the spin-orbit coupling between singlet and triplet excited states, causing a large electron density reduction on the conjugated system.[41-43] However, halogenation of conjugated molecules can also achieve useful properties from molecular packing to electrochemiluminescence for organic electronic and optoelectronic applications.[44,45] To reap the benefits of tuning molecular properties without a loss of FQY, we investigated a series of mono- and dihalogenated HBDI derivatives (F, Cl, Br, 2F, 2Cl, and 2Br-HBDI) in basic aqueous solution; halogenation sites are *ortho* to the phenolate oxygen (Fig. 1a,b insets). We employed steady-state UV/Visible absorption and fluorescence spectroscopy, femtosecond transient absorption (fs-TA), ground- and excited-state femtosecond stimulated Raman spectroscopy (GS and ES-FSRS, terminology used in literature),[46] and quantum calculations. The deprotonated chromophore responsible for the emissive state was strategically chosen to inhibit any ESPT that may be halogen-substituent-dependent (e.g., 2F, 2Br-HBDI),[40] and focus purely on the electrostatic and steric effects of the mono- and dihalogenation. The systematic addition of halogens increases the FQY in an anti-HAE fashion, allowing us to draw deep and interesting correlations between the ultrafast excited-state dynamics and emission properties.

Results and discussion

Steady-state electronic spectroscopy of the halogenated GFP chromophore derivatives reveals notable trends in fluorescence properties

The absorption and emission spectra of the anionic *p*-HBDI and its mono- and dihalogenated derivatives in pH=10 aqueous solution (Fig. 1) show similar spectral profiles and Stokes shifts, which are supported by computational results (Table 1). The frontier molecular orbitals (HOMO and LUMO) with electron density distribution from time-dependent density functional theory calculations (see Experimental Methods below for details) are largely consistent between the parent, mono-, and dihalogenated HBDI molecules (Fig. 2), confirming the nature of similar vertical electronic transitions.[18,32] The fluorinated HBDI derivatives exhibit the largest Stokes shifts amongst halogenated substituents (F>Cl>Br, 2F>2Cl>2Br), which could emanate from more intramolecular relaxation or better solvation of a planar fluorescent state (FS) than the chlorinated or brominated counterparts.[47] It remains challenging to predict the correlation between FQY and the Stokes shift, especially in molecules that are dominated by isomerization events starting from an electronic excited state. This is because, though a better solvated FS may enhance fluorescence, a larger Stokes shift could also mean more nonradiative decay pathways in competition along the way (see experimental results below).

Table 1 Steady-state electronic spectral properties of *p*-HBDI and its mono- and dihalogenated HBDI derivatives

Sample	Absorption /Emission (nm) [a]		Stokes Shift (cm^{-1})		pK_a (neu./ani.) [b]	FQY ($\times10^{-4}$) [c]	ε ($M^{-1}.cm^{-1}$) [d]	Brightness (%) [e]
	Exp.	Calc.	Exp.	Calc.				
p-HBDI	425/496	420/499	3,370	3,770	8.4	1.3	23,100	100
F-HBDI	422/498	421/502	3,620	3,830	6.9	1.4	22,000	105
Cl-HBDI	424/496	419/499	3,420	3,830	6.7	1.7	21,500	125
Br-HBDI	425/497	419/499	3,410	3,830	6.6	1.8	25,500	160
2F-HBDI	418/496	421/503	3,760	3,870	5.7	1.5	24,300	130
2Cl-HBDI	422/499	420/501	3,660	3,850	5.0	2.2	21,300	160
2Br-HBDI	423/500	421/501	3,640	3,790	4.9	2.3	25,000	200

[a] Measured from the experimental (Fig. 1) and calculated electronic spectral peaks of the anionic chromophores. Samples were prepared in pH=10 aqueous solution to ensure deprotonation. [b] Determined from titration curves (pH range from ca. 4–12) from the electronic absorption spectra of sample chromophores (Fig. S1 and S2 in the ESI†). neu., neutral; ani., anionic. [c] Φ, determined for the anionic chromophores upon 400 nm excitation (Fig. S3 in the ESI†). Coumarin 153 ($\lambda_{abs.}/\lambda_{em.}$ = 422/533 nm) was used as the standard (see Experimental methods section below). [d] Molar extinction coefficients as determined from the peak absorption values at 400 nm of sample chromophores with various concentrations (Fig. S4 in the ESI†). [e] The brightness as calculated by the product of FQY and molar extinction coefficient (i.e., brightness = Φ × ε). The percent brightness is relative to *p*-HBDI using the numerical values from Fig. S3 and S4.

The pK_a values of HBDI derivatives decrease from ~8.4 (parent *p*-HBDI) to 4.9–6.9 with the addition of various halogens on the chromophore P-ring (Table 1, also see titration curves in Fig. S1 and S2 in the ESI†) due to weakening of the phenolic O–H bond.[38,40] Although halogens are EWGs due to the inductive effect, they also act as weak EDGs due to the resonance effect. Fluorine is a stronger electron donor than chlorine and bromine since there is more *p*-orbital overlap with the nearest carbon on the conjugated P-ring; it is also the least ring-deactivating halogen, meaning it withdraws less electron density than the larger halogens. In turn, F places more electron density into the ring than Cl and Br, explaining the pK_a decrease in the order of –F > –Cl > –Br (Table 1).[48] The electron-donating capability is also reflected by the largest absorption energy of F-HBDI since the electrons are less delocalized in the ground state (S_0, hence a smaller "quantum box" with a larger electronic energy gap) than Cl- and Br-HBDI. The same trend follows for the dihalogenated HBDI derivatives, which exhibit lower pK_a values (increased inductive effects) and absorb at slightly higher energies (increased resonance effects) than their monohalogenated counterparts. Given the relative size similarity in these molecules leading to an approximately equal entropy change (Δ*S*), the pK_a drop reflects the decreased free energy change (Δ*G*) mainly due to the additional EWG-induced decrease in the enthalpy change (Δ*H*).[39,40]

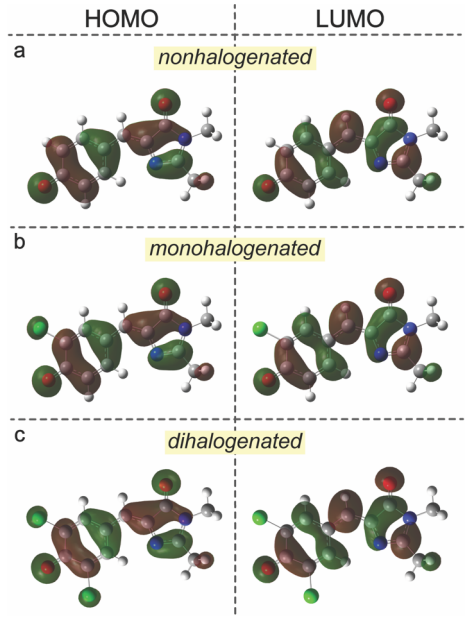

Fig. 2 Frontier molecular orbitals (FMOs) of HOMO and LUMO electron density distribution from quantum calculations of the (a) nonhalogenated/parent, (b) monohalogenated, and (c) dihalogenated HBDI derivatives. Due to similarity between three halogens in this work, chlorine was chosen to represent FMOs of the mono- and dihalogenated HBDI derivatives in (b) and (c). Red and green shades represent the positive and negative phases of electron density in the pertinent MOs with an isovalue of 0.02 $e/Å^3$.

Interestingly, despite low absolute values, the FQY increases with halogenation of the parent *p*-HBDI: mono(di)fluorination, mono(di)chlorination, mono(di)bromination increases the FQY by ca. 10(22)%, 34(73)%, and 42(84)%, respectively (Fig. S3 in the ESI†). Along with the molar extinction coefficient (Fig. S4 in the ESI†), this systematic evaluation reveals a clear increase in the overall brightness of halogenated HBDI derivatives relative to *p*-HBDI (Table 1). This finding directly contradicts the classic HAE, which states that upon addition of a covalently bound heavy atom or ion, the fluorescence is quenched while the phosphorescence yield is promoted due to an enhanced rate of intersystem crossing.[49,50] Typically, rigid molecules such as halogenated naphthalene and cytidines, amongst others, follow the classic HAE as the spin-orbit interactions are enhanced by halogenation.[50-53] In contrast, molecules that intrinsically possess dominant nonradiative energy deactivation pathways (e.g., isomerization) are more likely to exhibit anti-HAE behaviors (e.g., increased FQY upon addition of a heavy atom or ion), including the previously reported tetraphenylethene (TPE) and squaraine derivatives.[42,54] In particular, these molecular systems undergo ultrafast *cis-trans* photoisomerization with a common ~90° twisting about the methine bridge (in HBDI), ethylenic bond (in TPE), or polymethine bond (in squaraine) to pass through a nonadiabatic IC and/or CI from S_1 to S_0.[28,29,55-59]

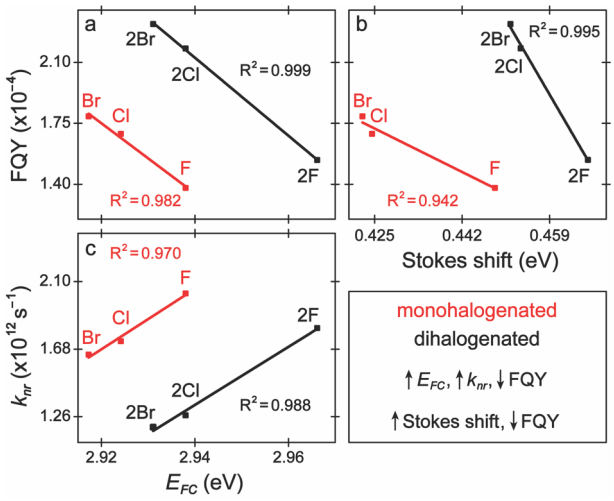

Fig. 3 Correlations between the emission properties and excited-state parameters. Plots of (a) FQY and (c) k_{nr} against E_{FC} (Franck-Condon energy; taken from the absorption peak maximum in Table 1) and (b) FQY against Stokes shift for the mono- (red) and di-halogenated (black) anionic HBDI derivatives exhibit a linear relationship. The R^2 values (color-coded) show strong correlations between these experimentally determined parameters as summarized in the lower right corner.

Such ultrafast processes are responsible for the essentially nonfluorescent nature of *p*-HBDI, and its derivatives, in solution (Table 1 and Fig. S3 in the ESI†).

To rationalize the FQY increase upon halogenation, the electrostatics of the P-ring substituent likely modify the excited-state potential energy surface (PES) mainly along the I-ring twisting coordinate, which requires the intrinsically coupled electronic and vibrational motions of the chromophore (see below).[18,29,60,61] Meanwhile, the inverted energy gap law (EGL) may provide some additional insights from an electronic perspective. The EGL, established from Fermi's golden rule, states that the nonradiative deactivation rate (k_{nr}) increases as the Franck-Condon energy (E_{FC}) decreases, thus leading to a lower FQY for typical rigid systems. On the contrary, the inverted EGL states that a high E_{FC} leads to high k_{nr} and low FQY.[62] From quantitative plots, we found strong correlations between the observed FQY and k_{nr} vs. E_{FC} (inverted EGL) and FQY vs. Stokes shift for the mono- and dihalogenated HBDI derivatives (Fig. 3). The simplified Strickler-Berg equation (Eq. 1)[63] was used to calculate the radiative deactivation rate, k_F,

$$k_{F,SB} = 4.34\times10^{7}(s^{-1}\cdot eV^{-2})\frac{E_F^3}{E_A}f \qquad \text{(Eq. 1)}$$

where E_F and E_A are the observed vertical emission and absorption peak energies (Table 1), and f is the oscillator strength of the emitting state, taken from time-dependent density functional theory (TD-DFT) calculations (Table S1 in the ESI†).[62,64] The definition of FQY (Eq. 2) can be used to determine k_{nr} from the FQY (Φ_F) and k_F (Eq. 3),

$$\Phi_F = \frac{k_F}{k_F+k_{nr}} \qquad \text{(Eq. 2)}$$

$$k_{nr} = (\frac{1}{\Phi_F}-1)k_F \qquad \text{(Eq. 3)}$$

The uncovered negative correlation between FQY and E_{FC}/Stokes shift, and positive correlation between k_{nr} and E_{FC} are intrinsic chromophore properties and can be elaborated as follows. First, nonradiative decay pathways dominate excited-state relaxation of the chromophore, which involves I- and/or P-ring twisting motions and access to an S_1/S_0 CI and/or IC channel (see below).[25,27,29,56] Second, we found a strong correlation (Fig. S5, ESI†) between FQY and the estimated 0–0 transition energy (TE) for absorption and emission (represented by the HOMO–LUMO energy gaps from TD-DFT calculations at different optimized structures in S_0 and S_1), though the trend is opposite to the experimental E_{FC} (Fig. 3a), which is likely due to limitations of DFT calculations in predicting the photoinduced charge transfer events and excitation energies.[47,64-66] Third, all the HBDI derivatives exhibit a similar magnitude of FQY and ultrafast access to the CI, allowing us to directly correlate an electronic FC descriptor (E_{FC}) with FQY because higher FC energies could enhance access to the S_1/S_0 CI through a small isomerization activation barrier, resulting in a larger Stokes shift (Fig. 3b), higher nonradiative relaxation rate constant (Fig. 3c), and lower FQY (e.g., –F < –Cl < –Br, Fig. 3a). In aggregate, although the absolute differences between the FQY, k_{nr}, E_{FC}, and Stokes shift values are small among various halogenated substituents, the strong correlation (R^2 ≥ 0.942) is hard to neglect for the two series of halogenation. Essentially, the apparent inverted EGL is intimately correlated with the excited-state PES of these "floppy" HBDI derivatives with a "conserved" twisting-induced operative unit (i.e., methine bridge) that undergo dominant ultrafast nonradiative energy dissipation including the *cis-trans* photoisomerization. This finding has motivated us to acquire more experimental evidence for the pertinent non-equilibrium structural motions using E_{FC} to guide the molecular system into a CI (via the I-ring twist) and/or an efficient IC process (via the P-ring twist) as detailed below.[28,29,32]

GS- and ES-FSRS characterization of the halogenated HBDI derivatives exposes key structural motions

The halogen-induced frequency shifts between the anionic *p*-HBDI and its mono- and dihalogenated HBDI derivatives in pH=10 aqueous solution were characterized by GS/ES-FSRS (Fig. 4). Using a combination of ps (narrowband) 550 nm Raman pump, fs (broadband) white-light probe, and fs actinic pump at 400 nm (see the Experimental methods section below for details), we obtained transient ES Raman signatures to contrast with their GS counterparts. Despite various combinations of the halogen substituents' electrostatic and steric properties in aqueous solution, the dominant GS conformation is the *cis* conformer as confirmed by systematic quantum calculations (Fig. S6, ESI†). Notably, the P-ring isomerization energy barrier is about half of the I-ring isomerization energy barrier at 90° bridge dihedral angle in the electronic ground state, in accord with previous quantum calculations on the *p*-HBDI anion in water.[27,60] Due to 550 nm Raman pump on the lower-energy side of 400 nm photoexcitation pulse that provides excessive energy (i.e., above the 0–0 energy gap, see Table 1),[29,31] we expect a better resonance Raman enhancement of the rapidly

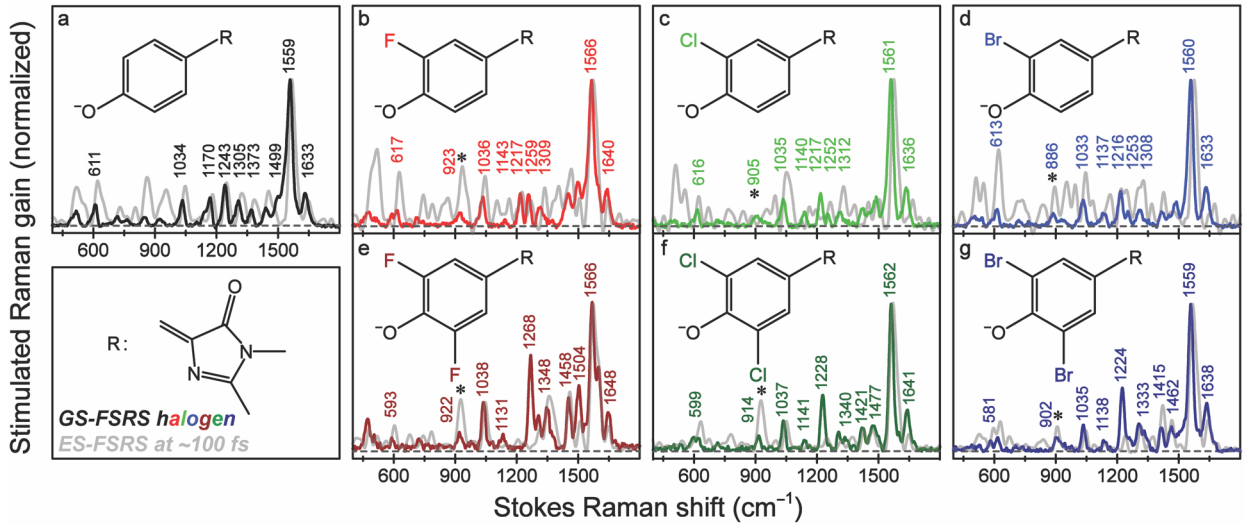

Fig. 4 Ground- and excited-state vibrational signatures of halogenated chromophores. GS-FSRS spectra of the anionic (a) *p*-HBDI, (b-d) mono-, and (e-g) dihalogenated HBDI derivatives in aqueous solution, all normalized at the peak near 1560 cm^{-1}. The chemical structure is displayed in each panel with the GS spectra color-coded to the substituent and ES spectra at ~100 fs in gray. R represents the remaining chromophore conjugated framework (lower left panel). Raman pump and actinic pump were tuned to 550 nm and 400 nm, respectively, with Raman probe on the Stokes side. The asterisks in panels b-g denote key carbon–halogen stretching modes (see Tables S2–S5 in the ESI†).

formed fluorescent state (FS, lower-lying than the initially populated FC state) wherein the excited-state Raman peaks can be clearly observed (Fig. 4).[29,31,38] Since the pertinent ultrafast timescale does not allow significant conformational motions, the observed GS and ES Raman peaks around the FC region (close to the GS equilibrated nuclear coordinates) are related to the composition of LUMO and HOMO (Fig. 2), implying modest electronic changes across the two-ring system and a rather localized C–X bond on the P ring (marked by asterisks in Fig. 4).[67] The main purpose of this series of FSRS characterization is thus spectral identification of an ultrafast ICT upon photoexcitation (e.g., frequency shift from $S_0 \rightarrow S_1$, see below)[29,60] and the vibrational mode frequency correlation with specific halogen substitutions on P ring of the anionic *p*-HBDI chromophore.[40,67]

Many of the ground state vibrational modes are largely conserved across the halogenated HBDI derivatives, such as ~610 and 1035 cm^{-1} modes with prominent I-ring deformation (see Tables S2 and S3 in the ESI†, also denoted in Fig. 4). The ~900, 1255, 1440, 1500, 1560, and 1640 cm^{-1} modes display a frequency shift upon varying the halogen substituent(s), and P ring constitutes a major contribution to the calculated normal modes. These results bespeak that P ring is more affected by halogenation than the bridge and I ring in the ground state, even though the molecule is conjugated. For several modes (>1480 cm^{-1}) with the phenolate CO stretching motion, a clear redshift from –F (2F), –Cl (2Cl), to –Br (2Br) can be understood for the same reasoning as the pK_a trend: F is a stronger electron donor than Cl and Br, so F places more electron density into the aromatic ring through the phenolate CO bond (a "conduit").

As a direct probe for halogenation, the C–X stretching motion of halogenated HBDI derivatives also exhibits a redshift from –F (mono, 923 cm^{-1}; di, 922 cm^{-1}), –Cl (mono, 905 cm^{-1}; di, 914 cm^{-1}), to –Br (mono, 886 cm^{-1}; di, 902 cm^{-1}), as expected from less *p*-orbital overlap with the carbon on the conjugated system for the bulkier halogens, which leads to a slightly lower bond order and longer bond length. The larger reduced mass of heavier halogens also contributes to the vibrational frequency redshift. The C–X stretch frequency and trend in Cl- and Br-HBDI correlate well with Cl- and Br-sfGFP; however, there is a slight (~4 cm^{-1}) redshift for the isolated halogenated chromophore, likely due to a more solvated local environment outside protein matrix.[67] The less significant redshift in dihalogenated HBDI derivatives for the symmetric C–X stretch is likely owing to cooperative motions from symmetric substituents at the *ortho* sites to the phenolate CO group (P ring). The general trend for the aforementioned modes that display a frequency shift upon varying the halogen substituent from F, Cl, to Br is a redshift, and they are enhanced upon electronic excitation due to an increase of polarizability (Fig. 4, see the asterisks).[31,51] These modes can therefore act as local probes for the site-specific halogenation of chromophores in condensed phases.[31,67]

The early-time (~100 fs) excited-state Raman spectra from ES-FSRS experiments show a clear frequency shift and peak broadening compared to the ground state (see Fig. 4, Tables S4

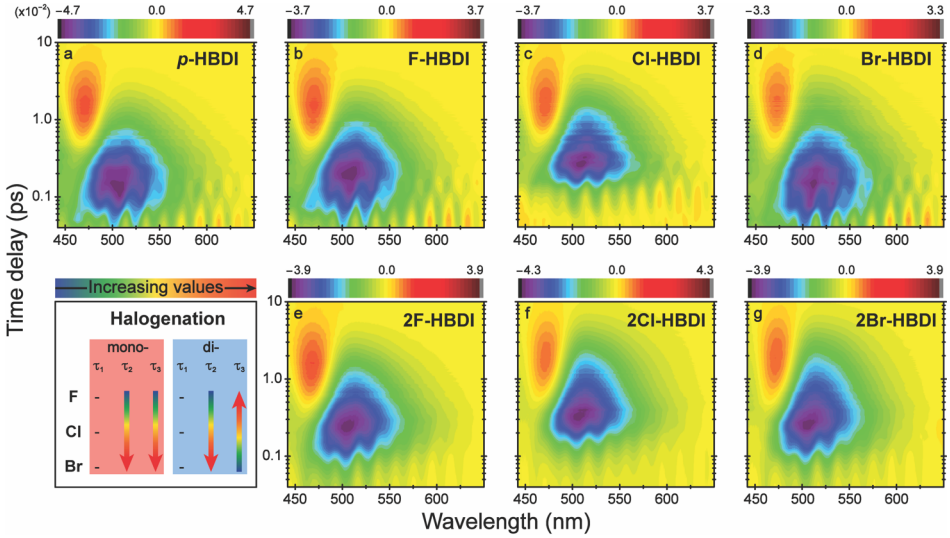

Fig. 5 Time-resolved electronic signatures of halogenated HBDI derivatives. Semilogarithmic contour plots of fs-TA spectra of the anionic (a) *p*-HBDI, (b-d) mono-, and (e-f) dihalogenated HBDI derivatives (halogen specified in each panel) in pH=10 aqueous solution after 400 nm excitation. The color bars are shown above; negative and positive values denote the SE and ESA bands, respectively. Slight deviations of time zero within ~100 fs have little effect on the kinetic analysis of TA marker bands. The trends in retrieved time constants (shown in increasing values from blue to red) for the mono- (red shade) and dihalogenated (blue shade) HBDI derivatives from global analysis are summarized in the lower left panel.

and S5 in the ESI†). The C–X stretching (~900 cm^{-1}) and the more delocalized (~1560 cm^{-1}) vibrational modes both show a blueshift from S_0 to S_1 (Tables S2–S5 in the ESI†) as the halogen size and polarizability increase (F < Cl < Br).[46,67] Notably, the dominant C=C/C=N stretching mode at ~1560 cm^{-1} is consistent with an earlier resonance Raman study using 369 nm excitation on anionic *p*-HBDI in basic ethanol,[68] an off-resonance Raman study using 752 nm excitation on a related *p*-HBDI model chromophore derivative in 5% (v/v) 1 M NaOH aqueous solution,[69] and our previous FSRS study using 550 nm Raman pump on anionic *p*-HBDI in pH=10 aqueous solution.[29] The frequency blueshift and intensity rise of these prominent marker bands upon electronic excitation likely originate from a combination of PES anharmonicity and electron redistribution. Since halogenation is a covalent modification, it could enable electrons (quantum in nature) to deviate from a classical conjugation system ("particle-in-a-box") through exchange interactions, especially in the deprotonated chromophores, thus affecting their ES vibrational features.[67,70] The subtle changes in the ground-state electronic absorption energies and geometrical conformations (Table 1 and Fig. S6 in the ESI†) and, concomitantly, the nonuniform change of Raman peaks near the FC region (Fig. 4) due to various halogen substituents imply that the electronic effects closely affect the observed vibrational motions.[31,71] Moreover, these Raman modes in S_1 (representative spectra in Fig. 4) show an intensity rise on the ~150 fs timescale without a noticeable peak frequency shift, supporting their assignment to the rapidly formed FS out of the FC region with a largely coplanar chromophore.[27,32,60]

For corroboration, our previous excited-state FSRS data up to 100 ps after 400 nm photoexcitation of anionic *p*-HBDI in water show initial peak frequency blueshift of the ~1570 cm^{-1} mode on the ~330 fs timescale and a longer redshift on the ~2 ps timescale due to FC/FS relaxation and TICT(I) barrier crossing, respectively.[29] Importantly, through detailed analysis of the S_1 vibrational intensity quantum beats, we uncovered anharmonic coupling between a delocalized ring out-of-plane bending mode at ~227 cm^{-1} and a delocalized in-plane ring stretching mode at ~1570 cm^{-1} which remains active from ~500 fs to 1.5 ps to guide the system into TICT(I) state where the CI locates. Notably, a delayed onset of this anharmonic coupling[29] suggests that the initially populated FC/FS modes (up to 500 fs) are not strongly coupled to the reactive isomerization coordinate.[26] Such energy transfer between high- and low-frequency vibrational modes is commonly expected to accompany the ultrafast FC relaxation and potential bifurcation of ensuing excited-state pathways (e.g., anionic *p*-HBDI and its halogenated derivatives, Fig. 4 and 5) to govern macroscopic functions (e.g., FQY, emission color, photostability, photoswitching) of the chromophore.[23,72-75]

Transient electronic spectroscopy elucidates the multidimensional PES from S_1 to S_0 with characteristic ring twist

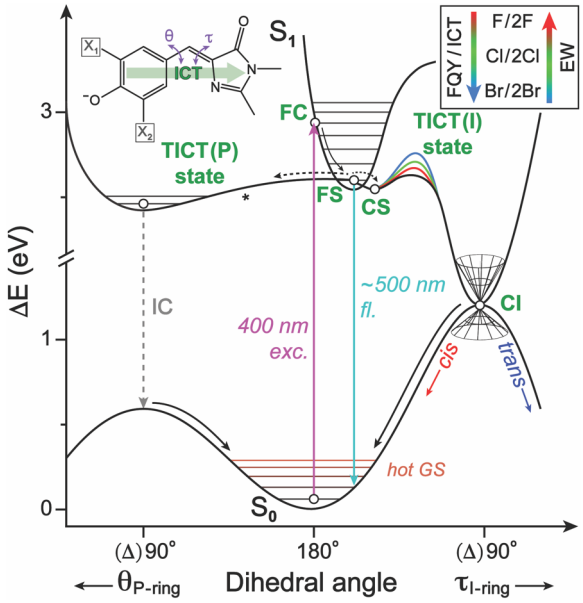

Fig. 6 Schematic of PES of anionic HBDI and its halogenated derivatives (color-coded according to the inset in the upper right corner) in aqueous solution after photoexcitation. Between the anharmonic PES with vibrational levels (horizontal bars, red denoting hot GS), vertical arrows represent 400 nm excitation (magenta), ~500 nm fluorescence (cyan), and internal conversion (gray). Dashed curved arrows in S_1 represent bifurcation of twisting coordinates along the τ and θ dihedral angles (defined in the chemical structure in upper left corner with the ICT route) which form TICT(I) and TICT(P) states, respectively. Barrier heights in S_0 were taken from quantum calculations (Fig. S6 in the ESI†), and the curved arrows depict chromophore relaxation in hot GS. The asterisk for the TICT(P) state formation indicates a minor component that could contribute to the observed TA features.

Given the contrasting HBDI derivatives with site-specific modifications (Fig. 1), fs-TA spectroscopy was systematically employed (see details in Experimental methods section below) to dissect the excited-state electronic dynamics of anionic *p*-HBDI as well as its mono- and dihalogenated HBDI derivatives in pH=10 aqueous solution following 400 nm photoexcitation (Fig. 5). Although spectral data were recorded up to 900 ps following photoexcitation, the 2D-contour plots only show pronounced SE and ESA features within ~10 ps, besides some weak features beyond this time (see global analysis results that retrieve a long time constant below). Due to spectral similarity and overlapping SE and ESA/hot GS absorption bands for various *p*-HBDI derivatives, global analysis was implemented to deconvolute the underlying dynamics/insights.[29,76] The evolution-associated difference spectra (EADS) with a conserved sequential kinetic model reveal three characteristic time constants: ~550 fs associated with initial relaxation remains relatively constant across all samples (black traces, Fig. S7 in the ESI†); 1.5–3 ps attributed to nonradiative relaxation through a CI and/or IC to reach a hot GS, which increases in the order of F < Cl < Br from mono- to dihalogenation (red traces, Fig. S7); and hundreds-of-ps to ns lifetime for hot-GS relaxation back to the thermally equilibrated GS (similar to *p*-HBDI),[29,69] which inversely increases and decreases from mono- to dihalogenation (i.e., F < Cl < Br vs. 2F > 2Cl ≈ 2Br) (blue traces, Fig. S7).

The chromophore excited-state population mainly slides out of the FC region via a steep slope (indicated by the TA dynamics, see below) and rapidly bifurcates along the I- or P-ring twisting coordinates at the lower portion, or the planar minimum (i.e., fluorescent state), of the initially accessed S_1 state.[32,60] The first temporal component from TA spectra (Fig. 5) shows a sub-ps lifetime, and is largely reminiscent of the fluorescence spectrum inverted (peak at ~500 nm with a long red tail that diminishes around 650 nm, similar to Fig. 1). Therefore, we could unambiguously assign this key transient electronic band to SE from the fluorescent state ("optically active" state with a planar structure, see Fig. S6 in the ESI† for the S_0 structure) that lies at the lower portion of the locally excited state.[60] In particular, we observed an ultrafast rise of the ~550 nm SE shoulder band (red-shifted from the main SE band at ~500 nm, see Fig. 5 and Fig. S7 in the ESI†), with a ~80 fs time constant for anionic *p*-HBDI and 60–110 fs for its halogenated derivatives in aqueous solution, all within the experimental cross-correlation time of ~120 fs. Therefore, the ultrafast appearance of a broad SE band within the instrument response time of our laser setup[29,40] and rapid evolution of the SE lineshape (black→red traces in Fig. S7, ESI†) is consistent with a steep PES slope out of the FC region leading to adjacent CT states (see below),[29,32,33,77] which accounts for the low FQY of these isolated chromophores in solution (Fig. 6).

There have been many theoretical calculations to support a near-barrierless nonradiative relaxation pathway along the P-ring twisting coordinate to form a twisted intramolecular charge transfer, TICT(P), state that leads to nonradiative IC process[28,32] and a nonradiative relaxation pathway along the I-ring twisting coordinate that must overcome a small energy barrier to form the TICT(I) state before encountering an S_1/S_0 CI.[33,60,77] The exact ring-twisting trajectories were shown to be dependent on the theory level, gas or solution phase,[32,60] polar or nonpolar solvents, electrostatics, charge distribution, and chromophore protonation state.[33,78,79] Notably, the imidazolinone bond photoisomerization in the *p*-HBDI anion with CT character has been commonly accepted as the major excited-state energy nonradiative relaxation pathway with a <2 kcal/mol activation barrier,[29,33,77,80] whereas no CI was generally found along the P-ring twisting coordinates (thus IC via an avoided crossing may occur).[30,81] These photoinduced ring-twisting motions lead to a hot GS, and we sketch the GS barrier heights directly from DFT calculation results (Fig. S6, ESI†). There has been continuous debates in the computational literature about the exact twisting coordinates in S_1 that facilitate the excited-state energy relaxation and molecular return to S_0, and the general consensus from high-level calculations is the TICT(I) state acting as the dominant pathway to achieve a fast and efficient internal conversion (IC) through a minimum energy (S_1/S_0) CI. There has been recent on-the-fly CASSCF surface hopping simulations[82] and XMS-CASPT2 surface hopping dynamics simulations[83] on the chromophore anion model *p*-HBI^- (no methyl groups on the I ring), respectively, *in vacuo*, so the calculated availability of an S_1/S_0 CI in TICT(P) besides TICT(I) may differ from the *p*-$HBDI^-$ in solution case (this work). It was also proposed from a time-resolved fluorescence study on anionic *p*-HBDI in various glycerol-water mixtures over a wide temperature range (from

room temperature to ~135 K below that) with nonexponential behavior that rotation of the phenyl ring paddle motion could allow a more facile swinging of the chromophore I ring into orientations that approach the CI (i.e., correlated motions during excited state relaxation).[27] In essence, the excited-state I-ring twisting coordinate, and a pertinent small energy barrier to the TICT(I) state that is modulated by the halogen-induced electrostatic effects across a two-ring system, could be primarily responsible for the anionic chromophore fluorescence and other energy dissipation in aqueous solution (Table 1).[27,29,33,77]

As we previously reported on the anionic *p*-HBDI in water, at very early times a prominent SE band appears (resembling the spontaneous emission band inverted, see Fig. 1 and 6) and rapidly decays and red-shifts with a ~500 fs lifetime. This transient feature is essentially related to the FQY and an intrinsic relationship between k_F and k_{nr} (Eq. 3), so the initial temporal component retrieved from fs-TA spectra represents an ephemeral fluorescent state (FS, see Fig. 5 and 6) with a characteristic lifetime of 520 fs in *p*-HBDI,[26,29] and 520–580 fs in the halogenated HBDI derivatives (Fig. S7 in the ESI†). This trend largely matches theoretical values from the aforementioned simplified Strickler-Berg equation (see Eq. 1) that predicts the dominant nonradiative transition lifetime (τ_{nr}) to be 430 fs and 494–837 fs in the halogenated HBDI derivatives (Table S1, ESI†).

Notably, the relative width of SE band in HBDI derivatives is much larger than the SE band of a similar chromophore embedded in the protein matrix (e.g., Ser-Tyr-Gly chromophore in the GFP-S205V mutant undergoing the photoinduced deprotonation to reach an anionic chromophore in S_1).[84] The broad SE band (Fig. 5) of HBDI chromophores thus arises from a relatively flat PES around the planar FS state (Fig. 6),[60,85] which could efficiently bifurcate into the CT-facilitated I- and P-ring twisting motions that exhibit distinct transient electronic features, including a redshift of the pronounced SE band.[31,86] This comparison also supports the importance of electrostatic effects on the fate of HBDI chromophores in condensed phase from the protein matrix[23,61,87] to aqueous solution.

To provide more insights into the photoinduced ICT process (Fig. 6 inset), the natural bond orbital (NBO) charges on the P-ring, methine bridge, and I-ring were calculated for the FC and FS states to estimate the amount of P-to-I-ring ICT (Table S6, ESI†). Interestingly, ICT seems to be enhanced from parent, mono-, to di-halogenated HBDI in the order of parent < F < Cl < Br < 2F < 2Cl ≈ 2Br, which largely correlates with the trend of an increasing second lifetime (1.6–2.8 ps) retrieved for the red trace from global analysis (Fig. S7, ESI†). The ESA on the blue side and SE on the red side represent a spectral signature of a TICT state of an anionic chromophore in solution,[29,86,88] which could involve efficient nonradiative relaxation through a nonadiabatic IC (P-ring twist) and an intermediate charge-separated (CS) state en route to the minimum energy CI,[29,33,60,77] corroborated by prominent SE band dynamics in fs-TA (Fig. 5). Accordingly, the halogen-induced electrostatic effects enhance ICT and stabilize the adjacent CS state (likely a rapid downhill process from the planar FS state on the sub-ps timescale), thus increasing the energy barrier en route to the S_1/S_0 CI (i.e., via the TICT(I) state, see Fig. 6 along the τ dihedral angle twisting coordinate). Meanwhile, the largely barrierless arrival at the TICT(P) state allows for efficient IC to the hot GS,[32,60,79] which becomes hindered as the halogen gets bulkier and heavier as P-ring substituents (see Fig. 6 along the θ dihedral angle). Previous temperature-dependent fluorescence studies on anionic *p*-HBDI with additional viscosity control (e.g., using glycerol-water mixtures over a temperature range of 147–282 K or basic ethanol from 77–295 K)[25,27] substantiated multiexponential fluorescence decay and the existence of a conversion barrier to TICT(I) along a nuclear coordinate that experiences weak solvent frictional forces. Given the overall structural similarity between the halogenated *p*-HBDI derivatives as well as the main chromophore torsional motion along its τ angle in water (Fig. 6), we depict the small energy barrier en route to the S_1/S_0 CI to be directly affected by the specific (mono- or di-) halogen substituents at the P ring via electronic effects.

Successful experimental attempts to increase the FQY of *p*-HBDI have been made by conformationally locking both rings through borylation[34,38] and by solely locking the P-ring.[89] However, the latter FQY enhancement was minimal (5.1×10^{-4}), suggesting that twisting along the I-ring coordinates primarily determines the extent of fluorescence through experimental validation. Recently, the excited-state electrostatic effects of EDG and EWG substituents on the GFP chromophore inside photoswitchable Dronpa2 were studied.[61] They found that I-ring isomerization is more energetically downhill for variants with increasing EWG substituents at similar *ortho*-positions to the phenolate oxygen site on the P-ring, which corroborates the aforementioned TA ps time constant increase as electron-withdrawing capability decreases, i.e., an energy barrier increase from –F, –Cl, to –Br (Fig. 6).[61] Previous calculations on the *p*-HBDI anion also predicted that main charge localization on P ring in the excited state promotes I-ring isomerization,[60] which is consistent with the much more negative charge on the P ring than I ring in both FC and FS states (Table S6, ESI†). However, some P-to-I-ring ICT upon photoexcitation could induce an enhanced P-ring twisting coordinate by increasing the negative charge on the I ring to some extent (Table S6).[27,60,83] The subsequent I-ring twist pathway could then promote ICT in the opposite direction (I-to-P-ring) to rebalance the charge and increase the chromophore basicity in S_1 (especially at the phenolate end).[35,61,79] Furthermore, the increasing energy barrier for halogenated *p*-HBDI derivatives can be rationalized by the Bell-Evans-Polanyi principle, which correlates the difference in activation energy (E_a) among the same molecular family to the difference of their reaction enthalpy (e.g., exothermicity), but there is also the kinetic stability that needs to be considered. For instance, the fluorinated HBDI derivatives (see Fig. 6, red barrier) experience the least energetically-hindered pathway to the CI in TICT(I) state with the shortest time constant (they also have the greatest E_{FC}, see Table 1 and Fig. 3). In contrast, the brominated species have the lowest E_{FC} and highest E_a on excited-state PES (Fig. 6, blue barrier).[30,62,90] This nice correlation between the halogen-dependent E_{FC} and the subsequent E_a along the excited-state relaxation pathway substantiates the aforementioned dominant electronic effects across the photoexcited chromophore's two-ring system.

Notably, all three of the aforementioned electrostatic phenomena cause an increase in E_a as the halogen substituent goes from F to Cl to Br, and 2F to 2Cl to 2Br, leading to an increase in FQY since the molecule becomes longer trapped in the excited state on ultrafast timescales (Fig. 6). In contrast, lengthening of the time constant for IC conversion from the TICT(P) state to reach a hot GS may be affected by both electrostatics and sterics, mainly due to a largely barrierless transition into the P-ring-twist pathway as an intrinsic property of the chromophore in both gas phase[28,32,33,80] and solution phase,[60] and halogens directly located on the P ring. After the CI passage via TICT(I) state, partial ICT from the I ring to P ring could induce back-isomerization in the hot GS, which would be more subject to sterics of the halogen as the time constant lengthens when the halogen size and amount increase (see the longest lifetime retrieved from TA spectra in Fig. S7, ESI†). Meanwhile, the pertinent ICT was shown to be much smaller in magnitude than its excited-state counterpart.[61] Consequently, the excited-state PES is likely dominated by electrostatics (Fig. 6, in S_1 state), whereas the ground-state PES with a downhill I-ring reverse twisting (starting from the CI) does not encounter a notable barrier and could be reflective of more steric effects.

Evidence for arrival at the hot GS from CI/IC is apparent in our ES-FSRS data (Fig. S8, ESI†). The delocalized P-ring C=C, C=O and I-ring C=N, C=O stretching motion is the most intense peak in GS (*p*-HBDI, 1559 cm^{-1}) and ES, wherein it rapidly blue-shifts (1568 cm^{-1}) upon photoexcitation, followed by weak Raman features around the CI/IC region[29] and reappearance at a red-shifted (1556 cm^{-1}) position on the hundreds-of-ps-to-ns timescale (Tables S2 and S4, ESI†). As we reported, the Raman peak intensity at late time is significantly less than that at early time, due to a still-twisted conformation with altered resonance conditions in the GS.[29] Therefore, the weak positive band at late times in global analysis can be assigned to hot GS absorption (Fig. S7 in the ESI†, blue trace) that is located on the red side of GS absorption peak (Fig. 1 and Table 1). Interestingly, the time constant trend for the molecular return to thermal equilibrium is inversely related to the mono- and di-halogenated species. Close inspection of the S_0 potential energy plotted against the bridge/exocyclic dihedral angles (two ring-twisting coordinates) from DFT calculations (Fig. S6 in the ESI†) shows that the GS barrier increases in the order of F < Cl < Br and from mono-to-dihalogenation along the I-ring twisting coordinate (Fig. S6b in the ESI†), whereas it decreases in the order F > Cl > Br and from mono-to-dihalogenation along the P-ring twisting coordinate (Fig. S6a in the ESI†). This systematic comparison indicates an interplay between electrostatics and sterics in S_0, which is largely consistent with the I-ring-twist pathway in S_1 (see barrier height trend in Fig. 6) but different from the P-ring-twist pathway in S_1 (essentially barrierless). For comparison, the halogen-substituted GFP chromophores in Dronpa2 also show the GS energy barrier increase in the order of F < Cl < Br.[61] We consider that this is more of a sterically-induced phenomenon, as opposed to electrostatics, due to the larger degree of bond rotation either along the I- or P-ring dihedral angles in S_0 than that in S_1 (e.g., ~30° along the I-ring twist coordinate[32,60,80] to reach the CS state en route to the TICT(I) barrier, see Fig. 6).

As the chromophore returns to original S_0 through isomerization and the I-to-P-ring ICT, water molecules also need to rearrange and stabilize the "regenerated" predominantly *cis* conformation.[91] For the parent and monohalogenated HBDI derivatives, the increasing time constant (400 ps, 440 ps, 930 ps, and 2.2 ns in Fig. S7a-d in the ESI†) could be due to sterics and slower solvation of the less symmetrical P-ring with the single heavy/bulky halogen adjacent to the phenolate oxygen site (see Fig. 6 inset). In contrast, the dihalogenated HBDI derivatives with two "balancing" halogens on the P-ring exhibit much more symmetry than their monohalogenated counterparts, which may allow for a largely conserved time constant of ~1 ns.[55] The slight reduction in GS barrier heights going from mono-to-dihalogenation upon P-ring twisting corroborates this interesting effect (Fig. S6a in the ESI†). The geometrically balanced dihalogenated HBDI derivatives may also lead to faster thermal relaxation (in 2Cl- and 2Br-HBDI) due to more effective collisions between the mobile P-ring and surrounding solvent molecules, hence the ~900 ps third time constant (Fig. S7f,g) vs. 2F-HBDI (1.2 ns, Fig. S7e in the ESI†).

Meanwhile, the effects of halogen bonding to the solvent molecules are likely minimal due to a strong EDG ($–O^-$) at the phenolate end of HBDI that effectively decreases the σ-hole size on the halogens (note that σ-hole stems from the positive electrostatic potential along the R–X bond), which would otherwise allow for the halogen "head-on" interactions with a Lewis base (e.g., a nucleophile like OH_2).[92] Systematic modification of the P-ring by exchanging the EDG (a hydroxy or $–O^-$) substituent to an EWG substituent, or by moving the halogens to a *meta* position, could enhance the halogen-bonding capabilities in this system. A future investigation about the effect of halogen bonds on the excited-state PES would be interesting as it may potentially hinder the P-ring twist,[35,89] modify the conjugated ring energetics across the two rings, further increase the FQY, or incorporate photoswitching capabilities into the molecular framework by exploiting the sequential activation of ICT-enabled ring twist on opposite ends of the chromophore with various EWGs/EDGs.[79,93,94]

Experimental methods

Synthesis and sample preparation

The *p*-HBDI compound was synthesized following previous procedures and used without further purification.[29,67] Detailed synthetic methods of the mono- and dihalogenated HBDI derivatives can be found in the ESI†. Aqueous solutions of various HBDI derivatives at pH=10 were prepared to ensure that the chromophore was in the anionic form for the ensuing spectral characterization at room temperature (see above).

Steady-state electronic spectroscopic characterization

The steady-state absorption measurements were taken with a Thermo Scientific Evolution 201 UV/Visible (UV/Vis) spectrophotometer with a 1-mm-pathlength quartz cuvette (Spectrosil 1-Q-1, Starna Cells). The fluorescence measurements were performed with a Shimadzu RF-6000

spectrofluorophotometer (λ_{ex}=400 nm) using a 5-mm-pathlength four-side rectangular quartz cuvette. Due to low fluorescence photon counts stemming from the essentially nonfluorescent nature of sample molecules, the excitation and emission slit widths were set to 10.0 nm with low sensitivity. Coumarin 153 has similar absorption and emission profiles as the HBDI derivatives studied and was thus used as the standard for FQY measurements using the relative method.[95] The linear regression and FQY values were determined systematically (Fig. S3 in the ESI†), wherein the fluorescence peak area was integrated from 485–635 nm for solutions having the optical density (OD) ranging from ~0.01–0.1.[96]

Time-resolved electronic and vibrational spectroscopic methods

Our ultrafast optical spectroscopy setup was built from a mode-locked Ti:Sapphire oscillator (Mantis-5, Coherent) that provides the seed for the regenerative amplifier (Legend Elite-USP-1K-HE, Coherent, Inc.). In brief, the fundamental laser output pulse train has ~800 nm center wavelength, 35 fs pulse duration, 3.7 mJ pulse energy, and 1 kHz repetition rate. The 400 nm actinic pump for the fs-TA and ES-FSRS measurements was produced via second harmonic generation of the laser fundamental, temporally compressed through a prism pair to produce ~100 fs laser pulses. A neutral density filter was used to reduce the pump power to ~0.4 mW for fs-TA measurements, and ~0.6 mW for ES-FSRS measurements. The actinic pump on/off ratio was obtained by an optical chopper that was synchronized to operate at half of the laser repetition rate (500 Hz).

The ps narrowband Raman pump used in the GS/ES-FSRS experiments was tuned to 550 nm with an average power of ~2.0 mW. A home-built second harmonic bandwidth compressor (SHBC) converts the 800 nm fs pulses to 400 nm ps pump pulses, while an fs noncollinear optical parametric amplifier (NOPA) with a grating-slit-based spectral filter generates the tunable ps seed. An ensuing home-built two-stage ps NOPA system performs amplification to produce the broadly tunable (ca. 480–720 nm) ps Raman pump.[46,97]

For both fs-TA and FSRS experiments, supercontinuum white light (SCWL) was used as the broadband probe. The probe pulse was generated by focusing a small portion of the laser fundamental output onto a 2-mm-thick quartz cuvette (Spectrosil 1-Q-2, Starna Cells) filled with deionized water, followed by compression via a chirped mirror pair (DCM-12, 400–700 nm, Laser Quantum, Inc.) to achieve <100 fs full-width-at-half-maximum (FWHM) of the pulse duration profile.[84] The incident Raman or TA pump and probe pulses were focused by a parabolic reflective mirror (*RFL* = 101.6 mm, MPD249-F01, Thorlabs, Inc.) onto the solution sample housed in a 1-mm-thick quartz cuvette (Spectrosil 1-Q-1, Starna Cells), equipped with a miniature magnetic staple bar to ensure a fresh sample spot being irradiated at each time delay point. The transmitted probe was spatially dispersed by a reflective grating (300 groves/mm, 300 nm blaze wavelength for fs-TA; and 1200 groves/mm, 500 nm blaze wavelength for FSRS) and focused onto an imaging spectrograph (IsoPlane SCT-320, Princeton Instruments, Inc.), before data collection via a front-illuminated and Lumogen-coated CCD array camera (PIXIS:100F, Princeton Instruments, Inc.). The detection time window for spectral data collection was set by the motorized translation stage (NRT150, Thorlabs, Inc.) to ~900 ps.[98]

The fs photoexcitation pulse at 400 nm for excited-state TA and FSRS experiments was strategically chosen due to strong sample absorption at that wavelength (Fig. 1) and simplicity of light conversion via second harmonic generation of the 800 nm fundamental laser output. The 550 nm ps Raman pump was selected due to its pre-resonance condition with the SE band (Fig. 5) to enhance the excited-state Raman features (Fig. 4).[29] The peak absorbance (optical density, OD) per mm was ~0.4 for fs-TA and ~1.5 for GS/ES-FSRS experiments. The UV/Vis spectrum of each sample was measured before and after each time-resolved experiment which showed minimal change (<5%) under the laser irradiation conditions used in ultrafast electronic and vibrational spectroscopy.[23,38]

Quantum calculations

The ground-state Raman mode frequencies were calculated using the density functional theory (DFT) method with the RB3LYP functional and 6-311G+(d,p) basis set of the geometrically optimized structure using Gaussian 09 software.[99] The total charge of each HBDI derivative was set at –1 due to the anionic chromophore (completely deprotonated) in pH=10 aqueous solution (Fig. S1 and S2 in the ESI†). The solvent water was modeled using the implicit integral equation formalism variant polarizable continuum model (IEFPCM). The calculated ground-state vibrational normal mode frequencies were multiplied by a frequency scaling factor of 0.985.[39,100] For vibrational normal mode frequency calculations at the geometrically optimized structure in the first singlet excited state (S_1), the frequency scaling factors of 0.97 for the high-frequency modes (>1000 cm^{-1}) and 1.01 for the low-frequency modes (<1000 cm^{-1}) were applied.[29,101] The vertical absorption and emission (Table 1) and frontier molecular orbitals showing electron density distribution (Fig. 2) were retrieved from the time-dependent (TD)-DFT energy calculations at the geometrically optimized ground-state structure using the same functional and basis sets as above. The first 20 excited states were calculated, and the UV/Vis peak FWHM is ~0.67 eV.

Conclusions

In summary, steady-state electronic spectroscopy, broadband fs-TA, GS/ES-FSRS, and quantum calculations were used in tandem to elucidate the excited-state energy relaxation pathways for a series of anionic halogenated HBDI derivatives in aqueous solution. In accordance with our recent "double-donor-one-acceptor" strategy,[18,36] halogenation increases the photoacidity from –F to –Cl to –Br, and from mono- to dihalogenation. The modest yet clear increase in FQY upon halogenation directly contradicts the classic HAE and is thus termed the anti-HAE effect, corroborated by other anti-HAE molecules that also possess a photoinduced ultrafast *cis-trans* isomerization pathway about methine or ethylenic bonds. The

primary events in excited state are revealed by the correlated TA (electronic) and FSRS (vibrational) features from the FC, FS, CS, to TICT states on ultrafast (fs-to-ps) timescales. In essence, this model system of GFP chromophore in aqueous solution represents a prime example of coupled electron and nuclear motions in governing the fate of a photoexcited molecule.

With a more quantitative evaluation of the excited-state energetics, we found a negative correlation between FQY and E_{FC}/Stokes shift, and a positive correlation between k_{nr} and E_{FC}. The corresponding τ_{nr} values largely match the apparent fluorescent state lifetime from global analysis of fs-TA spectra, which validates our interpretation of the experimental data and the proposed PES from FC region to FS state (dominated by nonradiative decay pathways). The increasing FQY also correlates with the increasing second time constant (1.7 to 2.8 ps for F-HBDI to Br-HBDI, and 1.8 to 2.7 ps for 2F-HBDI to 2Br-HBDI). An increase in the I-ring isomerization energy barrier, due to the halogen-induced electrostatics such as polarizability and ICT character starting from the P ring, correlates well with a slightly longer-lived excited state wherein more fluorescence occurs. On the contrary, hot-GS relaxation is primarily dictated by sterics of the substituent and symmetry of the P ring, on the hundreds-of-ps to ns timescales. Besides gaining fundamental insights into the photophysical reaction coordinates of a facile molecular machine, the biomimetic approach using the GFP chromophore also enables rational design (e.g., inhibition of ring-twisting motions with strategic substituents)[36,38,61,75] for brighter fluorophores in aqueous solution. We could envision the development of photochromic chemical probes with "on-demand" properties by engineering excited-state energetics and pathways through the site-specific halogenation and other functional substituents in bioimaging as well as medicinal fields, which commonly employ halogens during drug development.

Author Contributions

Conceptualization, C.F.; methodology, S.A.B., C.C., L.T., L.Z., N.S.B. and I.N.M.; software, S.A.B and L.T.; formal analysis, S.A.B. and C.C.; investigation, S.A.B., C.C., L.T. and C.F.; visualization, S.A.B. and C.F.; writing—original draft, S.A.B., C.C. and L.T.; writing—review and editing, C.F. and M.S.B; supervision, C.F.; funding acquisition, C.F. and M.S.B. All authors have read and agreed to the published version of the manuscript.

Conflicts of interest

There are no conflicts of interest to declare.

Acknowledgements

This work was supported by the NSF grants CHE-2003550 and MCB-1817949 (to C.F.) with additional lab personnel support provided by the NSF MRI grant DMR-1920368. The synthesis work was supported by Russian Foundation for Basic Research (RFBR) grant No. 20-33-70266 (to M.S.B.). We appreciate the OSU Chemistry Dorothy and Ramon Barnes Graduate Fellowship to S.A.B. (Summer 2020). We thank Taylor Krueger for the help with experiments and discussions.

Notes and references

1 O. Shimomura, F. H. Johnson and Y. Saiga, *J. Cell. Comp. Physiol.*, 1962, **59**, 223-239.
2 M. Chalfie, Y. Tu, G. Euskirchen, W. W. Ward and D. C. Prasher, *Science*, 1994, **263**, 802-805.
3 M. Ormö, A. B. Cubitt, K. Kallio, L. A. Gross, R. Y. Tsien and S. J. Remington, *Science*, 1996, **273**, 1392-1395.
4 R. Y. Tsien, *Annu. Rev. Biochem.*, 1998, **67**, 509-544.
5 A. Miyawaki, J. Llopis, R. Heim, J. M. McCaffery, J. A. Adams, M. Ikura and R. Y. Tsien, *Nature*, 1997, **388**, 882-887.
6 M. V. Matz, A. F. Fradkov, Y. A. Labas, A. P. Savitsky, A. G. Zaraisky, M. L. Markelov and S. A. Lukyanov, *Nat. Biotechnol.*, 1999, **17**, 969-973.
7 M. Zimmer, *Chem. Rev.*, 2002, **102**, 759-782.
8 N. C. Shaner, R. E. Campbell, P. A. Steinbach, B. N. G. Giepmans, A. E. Palmer and R. Y. Tsien, *Nat. Biotechnol.*, 2004, **22**, 1567-1572.
9 N. C. Shaner, M. Z. Lin, M. R. McKeown, P. A. Steinbach, K. L. Hazelwood, M. W. Davidson and R. Y. Tsien, *Nat. Methods*, 2008, **5**, 545-551.
10 M. W. Davidson and R. E. Campbell, *Nat. Methods*, 2009, **6**, 713-717.
11 D. Shcherbo, C. S. Murphy, G. V. Ermakova, E. A. Solovieva, T. V. Chepurnykh, A. S. Shcheglov, V. V. Verkhusha, V. Z. Pletnev, K. L. Hazelwood, P. M. Roche, S. Lukyanov, A. G. Zaraisky, M. W. Davidson and D. M. Chudakov, *Biochem. J.*, 2009, **418**, 567-574.
12 F. V. Subach and V. V. Verkhusha, *Chem. Rev.*, 2012, **112**, 4308-4327.
13 G. Jung, (Ed.), *Fluorescent Proteins I: From Understanding to Design*, Springer-Verlag, Berlin Heidelberg, 2012.
14 P. Dedecker, F. C. De Schryver and J. Hofkens, *J. Am. Chem. Soc.*, 2013, **135**, 2387-2402.
15 M. S. T. Gonçalves, *Chem. Rev.*, 2009, **109**, 190-212.
16 C. P. Toseland, *J. Chem. Biol.*, 2013, **6**, 85-95.
17 L. Yuan, W. Lin, K. Zheng, L. He and W. Huang, *Chem. Soc. Rev.*, 2013, **42**, 622-661.
18 C. Chen, M. S. Baranov, L. Zhu, N. S. Baleeva, A. Y. Smirnov, S. Zaitseva, I. V. Yampolsky, K. M. Solntsev and C. Fang, *Chem. Commun.*, 2019, **55**, 2537-2540.
19 A. Loudet and K. Burgess, *Chem. Rev.*, 2007, **107**, 4891-4932.
20 E. Kim, M. Koh, B. J. Lim and S. B. Park, *J. Am. Chem. Soc.*, 2011, **133**, 6642-6649.
21 M. Chattoraj, B. A. King, G. U. Bublitz and S. G. Boxer, *Proc. Natl. Acad. Sci. U. S. A.*, 1996, **93**, 8362-8367.
22 K. Brejc, T. K. Sixma, P. A. Kitts, S. R. Kain, R. Y. Tsien, M. Ormö and S. J. Remington, *Proc. Natl. Acad. Sci. U. S. A.*, 1997, **94**, 2306-2311.
23 C. Fang, R. R. Frontiera, R. Tran and R. A. Mathies, *Nature*, 2009, **462**, 200-204.
24 S. R. Meech, *Chem. Soc. Rev.*, 2009, **38**, 2922-2934.
25 N. M. Webber, K. L. Litvinenko and S. R. Meech, *J. Phys. Chem. B*, 2001, **105**, 8036-8039.
26 D. Mandal, T. Tahara and S. R. Meech, *J. Phys. Chem. B*, 2004, **108**, 1102-1108.
27 R. Gepshtein, D. Huppert and N. Agmon, *J. Phys. Chem. B*, 2006, **110**, 4434-4442.

28 A. Svendsen, H. V. Kiefer, H. B. Pedersen, A. V. Bochenkova and L. H. Andersen, *J. Am. Chem. Soc.*, 2017, **139**, 8766-8771.
29 M. A. Taylor, L. Zhu, N. D. Rozanov, K. T. Stout, C. Chen and C. Fang, *Phys. Chem. Chem. Phys.*, 2019, **21**, 9728-9739.
30 A. Follenius-Wund, M. Bourotte, M. Schmitt, F. Iyice, H. Lami, J.-J. Bourguignon, J. Haiech and C. Pigault, *Biophys. J.*, 2003, **85**, 1839-1850.
31 C. Fang, L. Tang and C. Chen, *J. Chem. Phys.*, 2019, **151**, 200901.
32 M. E. Martin, F. Negri and M. Olivucci, *J. Am. Chem. Soc.*, 2004, **126**, 5452-5464.
33 I. V. Polyakov, B. L. Grigorenko, E. M. Epifanovsky, A. I. Krylov and A. V. Nemukhin, *J. Chem. Theory Comput.*, 2010, **6**, 2377-2387.
34 M. S. Baranov, K. A. Lukyanov, A. O. Borissova, J. Shamir, D. Kosenkov, L. V. Slipchenko, L. M. Tolbert, I. V. Yampolsky and K. M. Solntsev, *J. Am. Chem. Soc.*, 2012, **134**, 6025-6032.
35 H. Deng, C. Yu, L. Gong and X. Zhu, *J. Phys. Chem. Lett.*, 2016, **7**, 2935-2944.
36 C. Chen and C. Fang, *Chem. Asian J.*, 2020, **15**, 1514-1523.
37 R. Simkovitch, S. Shomer, R. Gepshtein and D. Huppert, *J. Phys. Chem. B*, 2015, **119**, 2253-2262.
38 C. Chen, W. Liu, M. S. Baranov, N. S. Baleeva, I. V. Yampolsky, L. Zhu, Y. Wang, A. Shamir, K. M. Solntsev and C. Fang, *J. Phys. Chem. Lett.*, 2017, **8**, 5921–5928.
39 C. Chen, L. Zhu, M. S. Baranov, L. Tang, N. S. Baleeva, A. Y. Smirnov, I. V. Yampolsky, K. M. Solntsev and C. Fang, *J. Phys. Chem. B*, 2019, **123**, 3804-3821.
40 C. Chen, L. Zhu, S. A. Boulanger, N. S. Baleeva, I. N. Myasnyanko, M. S. Baranov and C. Fang, *J. Chem. Phys.*, 2020, **152**, 021101.
41 D. F. Eaton, *J. Am. Chem. Soc.*, 1981, **103**, 7235-7239.
42 P. Xu, Q. Qiu, X. Ye, M. Wei, W. Xi, H. Feng and Z. Qian, *Chem. Commun.*, 2019, **55**, 14938-14941.
43 K. E. Oberhofer, M. Musheghyan, S. Wegscheider, M. Wörle, E. D. Iglev, R. D. Nikolova, R. Kienberger, P. S. Pekov and H. Iglev, *RSC Adv.*, 2020, **10**, 27096-27102.
44 M. L. Tang and Z. Bao, *Chem. Mater.*, 2011, **23**, 446-455.
45 C.-L. Sun, J. Li, H.-W. Geng, H. Li, Y. Ai, Q. Wang, S.-L. Pan and H.-L. Zhang, *Chem. Asian J.*, 2013, **8**, 3091-3100.
46 W. Liu, Y. Wang, L. Tang, B. G. Oscar, L. Zhu and C. Fang, *Chem. Sci.*, 2016, **7**, 5484-5494.
47 G. Haberhauer, R. Gleiter and C. Burkhart, *Chem. Eur. J.*, 2016, **22**, 971-978.
48 J. Rosenthal and D. I. Schuster, *J. Chem. Educ.*, 2003, **80**, 679-690.
49 D. S. McClure, *J. Chem. Phys.*, 1949, **17**, 905-913.
50 J. Al Anshori, T. Slanina, E. Palao and P. Klán, *Photochem. Photobiol. Sci.*, 2016, **15**, 250-259.
51 J. C. Miller, J. S. Meek and S. J. Strickler, *J. Am. Chem. Soc.*, 1977, **99**, 8175-8179.
52 S. Sarkar, H. P. Hendrickson, D. Lee, F. DeVine, J. Jung, E. Geva, J. Kim and B. D. Dunietz, *J. Phys. Chem. C*, 2017, **121**, 3771-3777.
53 R. Xu, Z. Hu, X. Wang, Y. Liu, Z. Zhou, J. Xu, Z. Sun, H. Sun and J. Chen, *J. Phys. Chem. B*, 2020, **124**, 2560-2567.
54 U. Mayerhöffer, B. Fimmel and F. Würthner, *Angew. Chem. Int. Ed.*, 2012, **51**, 164-167.
55 F. Momicchioli, A. S. Tatikolov, D. Vanossi and G. Ponterini, *Photochem. Photobiol. Sci.*, 2004, **3**, 396-402.
56 B. G. Levine and T. J. Martínez, *Annu. Rev. Phys. Chem.*, 2007, **58**, 613-634.
57 G.-J. Zhao, K.-L. Han, Y.-B. Lei and Y.-S. Dou, *J. Chem. Phys.*, 2007, **127**, 094307.
58 A. Prlj, N. Došlić and C. Corminboeuf, *Phys. Chem. Chem. Phys.*, 2016, **18**, 11606-11609.
59 Y.-J. Gao, X.-P. Chang, X.-Y. Liu, Q.-S. Li, G. Cui and W. Thiel, *J. Phys. Chem. A*, 2017, **121**, 2572-2579.
60 P. Altoè, F. Bernardi, M. Garavelli, G. Orlandi and F. Negri, *J. Am. Chem. Soc.*, 2005, **127**, 3952-3963.
61 M. G. Romei, C.-Y. Lin, I. I. Mathews and S. G. Boxer, *Science*, 2020, **367**, 76-79.
62 J. Shi, M. A. Izquierdo, S. Oh, S. Y. Park, B. Milián-Medina, D. Roca-Sanjuán and J. Gierschner, *Org. Chem. Front.*, 2019, **6**, 1948-1954.
63 S. J. Strickler and R. A. Berg, *J. Chem. Phys.*, 1962, **37**, 814-822.
64 J. Shi, L. E. Aguilar Suarez, S.-J. Yoon, S. Varghese, C. Serpa, S. Y. Park, L. Lüer, D. Roca-Sanjuán, B. Milián-Medina and J. Gierschner, *J. Phys. Chem. C*, 2017, **121**, 23166-23183.
65 H. Iikura, T. Tsuneda, T. Yanai and K. Hirao, *J. Chem. Phys.*, 2001, **115**, 3540-3544.
66 M. A. Rohrdanz, K. M. Martins and J. M. Herbert, *J. Chem. Phys.*, 2009, **130**, 054112.
67 B. G. Oscar, L. Zhu, H. Wolfendeen, N. D. Rozanov, A. Chang, K. T. Stout, J. W. Sandwisch, J. J. Porter, R. A. Mehl and C. Fang, *Front. Mol. Biosci.*, 2020, **7**, 131.
68 P. Schellenberg, E. Johnson, A. P. Esposito, P. J. Reid and W. W. Parson, *J. Phys. Chem. B*, 2001, **105**, 5316-5322.
69 A. F. Bell, X. He, R. M. Wachter and P. J. Tonge, *Biochemistry*, 2000, **39**, 4423-4431.
70 C.-Y. Lin and S. G. Boxer, *J. Phys. Chem. B*, 2020, **124**, 9513-9525.
71 K. A. Nguyen, P. N. Day and R. Pachter, *J. Chem. Phys.*, 1999, **110**, 9135-9144.
72 M. Liebel, C. Schnedermann, G. Bassolino, G. Taylor, A. Watts and P. Kukura, *Phys. Rev. Lett.*, 2014, **112**, 238301.
73 P. J. M. Johnson, A. Halpin, T. Morizumi, V. I. Prokhorenko, O. P. Ernst and R. J. D. Miller, *Nat. Chem.*, 2015, **7**, 980-986.
74 D. P. Hoffman and R. A. Mathies, *Acc. Chem. Res.*, 2016, **49**, 616-625.
75 C. Fang and L. Tang, *Annu. Rev. Phys. Chem.*, 2020, **71**, 239-265.
76 R. Berera, R. van Grondelle and J. M. Kennis, *Photosynth. Res.*, 2009, **101**, 105-118.
77 S. Olsen and S. C. Smith, *J. Am. Chem. Soc.*, 2008, **130**, 8677-8689.
78 J.-S. Yang, G.-J. Huang, Y.-H. Liu and S.-M. Peng, *Chem. Commun.*, 2008, 1344-1346.
79 S. Olsen, K. Lamothe and T. J. Martínez, *J. Am. Chem. Soc.*, 2010, **132**, 1192-1193.
80 A. V. Bochenkova and L. H. Andersen, *Faraday Discuss.*, 2013, **163**, 297-319.
81 T. Kumpulainen, B. Lang, A. Rosspeintner and E. Vauthey, *Chem. Rev.*, 2017, **117**, 10826-10939.
82 L. Zhao, P.-W. Zhou, B. Li, A.-H. Gao and K.-L. Han, *J. Chem. Phys.*, 2014, **141**, 235101.
83 J. W. Park and T. Shiozaki, *J. Chem. Theory Comput.*, 2017, **13**, 3676-3683.
84 L. Tang, L. Zhu, M. A. Taylor, Y. Wang, S. J. Remington and C. Fang, *Molecules*, 2018, **23**, 2226.
85 J. Lee, J. R. Challa and D. W. McCamant, *J. Phys. Chem. B*, 2017, **121**, 4722–4732.
86 L. Tang and C. Fang, *J. Phys. Chem. B*, 2019, **123**, 4915-4928.
87 J. W. Park and Y. M. Rhee, *J. Am. Chem. Soc.*, 2016, **138**, 13619-13629.
88 S. Sasaki, G. P. C. Drummen and G.-i. Konishi, *J. Mater. Chem. C*, 2016, **4**, 2731-2743.

89 Y.-H. Hsu, Y.-A. Chen, H.-W. Tseng, Z. Zhang, J.-Y. Shen, W.-T. Chuang, T.-C. Lin, C.-S. Lee, W.-Y. Hung, B.-C. Hong, S.-H. Liu and P.-T. Chou, *J. Am. Chem. Soc.*, 2014, **136**, 11805-11812.

90 W. P. Jencks, *Chem. Rev.*, 1985, **85**, 511-527.

91 X. He, A. F. Bell and P. J. Tonge, *FEBS Lett.*, 2003, **549**, 35-38.

92 M. V. Chernysheva, M. Bulatova, X. Ding and M. Haukka, *Cryst. Growth Des.*, 2020, **20**, 7197-7210.

93 D. Bourgeois and V. Adam, *IUBMB Life*, 2012, **64**, 482-491.

94 W. Szymański, J. M. Beierle, H. A. V. Kistemaker, W. A. Velema and B. L. Feringa, *Chem. Rev.*, 2013, **113**, 6114-6178.

95 T. D. Krueger, S. A. Boulanger, L. Zhu, L. Tang and C. Fang, *Struct. Dyn.*, 2020, **7**, 024901.

96 K. Rurack and M. Spieles, *Anal. Chem.*, 2011, **83**, 1232-1242.

97 L. Zhu, W. Liu and C. Fang, *Appl. Phys. Lett.*, 2014, **105**, 041106.

98 S. R. Tachibana, L. Tang, C. Chen, L. Zhu, Y. Takeda, K. Fushimi, T. K. Seevers, R. Narikawa, M. Sato and C. Fang, *Spectrochim. Acta A*, 2021, **250**, 119379.

99 M. J. Frisch, G. W. Trucks, H. B. Schlegel, G. E. Scuseria, M. A. Robb, J. R. Cheeseman, G. Scalmani, V. Barone, B. Mennucci, G. A. Petersson, H. Nakatsuji, M. Caricato, X. Li, H. P. Hratchian, A. F. Izmaylov, J. Bloino, G. Zheng, J. L. Sonnenberg, M. Hada, M. Ehara, K. Toyota, R. Fukuda, J. Hasegawa, M. Ishida, T. Nakajima, Y. Honda, O. Kitao, H. Nakai, T. Vreven, J. J. A. Montgomery, J. E. Peralta, F. Ogliaro, M. Bearpark, J. J. Heyd, E. Brothers, K. N. Kudin, V. N. Staroverov, R. Kobayashi, J. Normand, K. Raghavachari, A. Rendell, J. C. Burant, S. S. Iyengar, J. Tomasi, M. Cossi, N. Rega, J. M. Millam, M. Klene, J. E. Knox, J. B. Cross, V. Bakken, C. Adamo, J. Jaramillo, R. Gomperts, R. E. Stratmann, O. Yazyev, A. J. Austin, R. Cammi, C. Pomelli, J. W. Ochterski, R. L. Martin, K. Morokuma, V. G. Zakrzewski, G. A. Voth, P. Salvador, J. J. Dannenberg, S. Dapprich, A. D. Daniels, Ö. Farkas, J. B. Foresman, J. V. Ortiz, J. Cioslowski and D. J. Fox, *Gaussian 09, Revision B.1*, Gaussian, Inc., Wallingford, CT, 2009.

100 A. P. Scott and L. Radom, *J. Phys. Chem.*, 1996, **100**, 16502-16513.

101 J. P. Merrick, D. Moran and L. Radom, *J. Phys. Chem. A*, 2007, **111**, 11683-11700.